JOURNAL OF COMPUTATIONAL PHYSICS 106, 155–175 (1993)

Wavelets and the Numerical Solution of Partial Differential Equations*

SAM QIAN AND JOHN WEISS

Aware, Inc., One Memorial Drive, Cambridge, Massachusetts 02142

Received March 27, 1992

We present a new numerical method for the solution of partial differential equations in nonseparable domains. The method uses a wavelet–Galerkin solver with a nontrivial adaptation of the standard capacitance matrix method. The numerical solutions exhibit spectral convergence with regard to the order of the compactly supported, Daubechies wavelet basis. Furthermore, the rate of convergence is found to be independent of the geometry. We solve the Helmholtz equation since, for variations in the parameter, the solutions have qualitative properties that well illustrate the applications of our method. © 1993 Academic Press, Inc.

1. INTRODUCTION

In this paper we examine the feasibility of applying wavelet based numerical methods to the solution of partial differential equations. Specifically, we compare the wavelet–Galerkin method to standard numerical methods for the numerical solution of the biharmonic Helmholtz equation and the reduced wave equation in nonseparable, two-dimensional geometry.

We use compactly supported wavelets as a Galerkin basis and develop a wavelet–capacitance matrix method to handle boundary geometry. We have developed an extension of the standard capacitance matrix method that greatly reduces the numerical residual errors. In contrast with the standard method, our method shows fast, even spectral, convergence at relatively coarse levels of discretization. Furthermore, for comparable levels of discretization the rates of convergence appear to be independent of the geometry. For several geometries we have made a detailed comparison of methods, examining accuracy and rates of convergence. We have also developed least-square versions of our algorithm for the Helmholtz equation in nonseparable geometries and examined the accuracy and convergence of these methods.

In Section 2 we present the wavelet–Galerkin method for partial differential equations. To illustrate this discussion, several applications to nonlinear partial differential equations with periodic boundary conditions are reviewed. The periodic wavelet–Galerkin solver is an essential component of our method. We examine the rates of convergence of this solver when applied to the Helmholtz equation.

In Section 3 we develop the wavelet–capacitance method for solving partial differential equations in nonseparable geometry. In Section 4 we then apply the method to the numerical solution of the Helmholtz equation in two-dimensional domains. Detailed results with comparison to standard methods are presented for the L-shaped region.

We have also examined the use of symmetry in our method. In Section 6 several useful results are presented that can be developed to reduce the level of required computation. In summary, our numerical study of the Helmholtz equation shows that:

- The wavelet–Galerkin/capacitance matrix method (the wavelet–capacitance matrix method) is stable and *spectrally* accurate. These results apply to general nonseparable domains and all ranges of the parameters.
- The wavelet algorithm is found to obtain accurate results for problems where, for instance, finite difference methods do not converge, or converge slowly, and where Fourier spectral methods do not apply.
- For a fixed level of discretization, increasing the order of the wavelet basis spectrally decreases the error.
- The rates of convergence in sup norm appear to depend on the wavelet basis, DN, and discretization, δx, as $(\delta x)^{N-5}$.
- The rates of convergence in sup norm appear to be independent of the domain shape.
- Least-square versions of the wavelet algorithm can preserve accuracy and decrease the computation by more than a factor of four. The finite difference algorithms would not allow effective least-square implementations.

Furthermore,

- All errors (accuracy and convergence) are measured in the pointwise sup norm.

* The U.S. Government's right to retain a nonexclusive royalty-free license in and to the copyright covering this paper, for governmental purposes, is acknowledged.

0021-9991/93 $5.00
Copyright © 1993 by Academic Press, Inc.
All rights of reproduction in any form reserved.

• Our implementation is fast, since it is based on fast (FFT) evaluations for periodic geometry adapted to nonseparable geometry.

• The basic algorithm applies to one, two, and three space dimensions, without essential modification.

• The wavelet–Galerkin method preserves symmetries of the domain and defines a type of discrete orthogonality that is very useful for further applications of the method. These applications include fast domain decomposition techniques.

• To our knowledge, our algorithm is a unique extension of the classical capacitance–matrix method and should have several and diverse applications to problems requiring a higher order accuracy.

2. THE WAVELET–GALERKIN METHOD

Compactly supported wavelets have several properties that are quite useful for representing solutions of PDEs [6, 10, 16]. The orthogonality, compact support, and exact representation of polynomials of a fixed degree allow the efficient and stable calculation of regions with strong gradients or oscillations. For instance, we have applied wavelets to problems of shock capture. The general method is a straightforward adaptation of the Galerkin procedure with a wavelet basis [6, 10, 16].

The compact wavelets have a finite number of derivatives and the derivatives, when they exist, can be highly oscillatory. This makes the numerical evaluation of integrals difficult and unstable. We have found methods for the evaluation of functionals on wavelet bases [9]. Comparison with standard numerical results demonstrates that these procedures are critical for the wavelet methods, especially as applied to nonlinear problems.

2.1. *Compactly Supported Wavelets*

Ingrid Daubechies defined the class of compactly supported wavelets [4]. Briefly, let φ be a solution of the *scaling* relation

$$\varphi(x)=\sum_k a_k \varphi(2x-k).$$

The a_k are a collection of coefficients that categorize the specific wavelet basis. The expression φ is called the scaling function.

The associated *wavelet* function ψ is defined by the equation

$$\psi(x)=\sum_k (-1)^k a_{1-k}\varphi(2x-k).$$

The normalization $\int \varphi\, dx = 1$ of the scaling function obtains the condition

$$\sum_k a_k = 2.$$

The translates of φ are required to be orthonormal

$$\int \varphi(x-k)\,\varphi(x-m)=\delta_{k,m}.$$

From the scaling relation this implies the condition

$$\sum_{k=0}^{N-1} a_k a_{k-2m}=\delta_{0m}.$$

For coefficients verifying the above two conditions, the functions consisting of translates and dilations of the wavelet function, $\psi(2^j x-k)$, form a complete, orthogonal basis for square integrable functions on the real line, $L^2(R)$.

If only a finite number of the a_k are nonzero then φ will have compact support. Since

$$\int \varphi(x)\,\psi(x-m)\,dx=\sum_k (-1)^k a_{1-k}a_{k-2m}=0,$$

the translates of the scaling function and wavelet define orthogonal subspaces

$$V_j=\{2^{j/2}\varphi(2^j x-m);\ m=\ldots,-1,0,1,\ldots\},$$
$$W_j=\{2^{j/2}\psi(2^j x-m);\ m=\ldots,-1,0,1,\ldots\}.$$

The relation

$$V_{j+1}=V_j\oplus W_j$$

implies the Mallat transform [4]

$$V_0\subset V_1\subset\cdots\subset V_{j+1},$$
$$V_{j+1}=V_0\oplus W_0\oplus W_1\oplus\cdots\oplus W_j.$$

Smooth scaling functions arise as a consequence of the degree of approximation of the translates. The conditions that the polynomials $1, x, \ldots, x^{p-1}$ be expressed as linear combinations of the translates of $\varphi(x-k)$ is implied by the conditions

$$\sum_k (-1)^k k^m a_k = 0$$

for $m=0, 1, \ldots, p-1$. The following are equivalent results [15]:

- $\{1, x, \ldots, x^{p-1}\}$ are linear combinations of $\varphi(x-k)$.
- $\|f-\sum c_k\varphi(2^j x-k)\|\leqslant C2^{-jp}\,\|f^{(p)}\|$, where $c_k=\int f(x)\,\varphi(2^j x-k)\,dx$.
- $\int x^m\psi(x)\,dx=0$ for $m=0, 1, \ldots, p-1$.
- $\int f(x)\,\psi(2^j x)\,dx\leqslant c2^{-jp}$
- L_N, where $L_{i,j}=a_{2i-j}$ has eigenvalues $1, \frac{1}{2}, \ldots, (\frac{1}{2})^{p-1}$.

For the Daubechies scaling/wavelet function DN we have $p=N/2$.

In Fig. 1 we see pictured an example of a compactly supported scaling function and its associated fundamental wavelet function. By rescaling and translation we obtain a complete orthonormal system for $L^2(\mathbf{R})$ which has sufficient smoothness to also be a basis for $H^1(\mathbf{R})$. This wavelet system then yields a basis for solution methods for second-order elliptic boundary problems on intervals on the real line. The illustrated example, which is due to Daubechies [4], has fundamental support $[0, 5]$. For arbitrarily large even N there is a Daubechies example of a fundamental scaling function defining a wavelet family with fundamental support in the interval $[0, N-1]$ [4]. Wavelet bases of arbitrarily high order of smoothness can be constructed in this way, but the order of smoothness is bounded by the length of the support.

2.2. *The Wavelet–Galerkin Method*

For a PDE of the form

$$F(U, U_t, ..., U_x, U_{xx}, ...) = 0$$

define the wavelet expansion

$$U = \sum U_k \varphi(x-k).$$

An approximation to the solution is defined by

$$\hat{U} = \sum_{k=-M}^{N} \hat{U}_k \varphi(x-k).$$

In effect, the solution is projected onto the subspace spanned by

$$\Phi(M, N) = \{\varphi(x-k) : k = -M, ..., N\}.$$

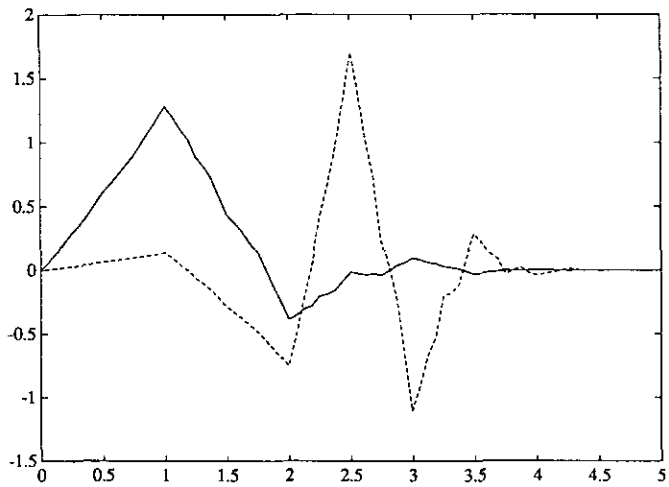

FIG. 1. Daubechies' scaling and wavelet functions for $N=6$ with support on $[0, 5]$.

To determine the coefficients of this expansion we substitute into the equation and again project the resulting expression onto the subspace $\Phi(M, N)$. This uniquely determines the coefficients U_k. Here we assume, without loss of generality, that the integers represent the finest scale of variation and the period scales with the number of translates. This simplifies the relevant calculations and can be implemented by a simple change of variable $y = 2^j x$.

The projection requires $\hat{U}_k$ to verify the equations

$$\int_{-\infty}^{\infty} \varphi(x-k)\, F(\hat{U}, \hat{U}_t, \hat{U}_x, ...)\, dx = 0$$

for $k = -M, ..., N$. To evaluate this expression we must know the coefficients of the form

$$\int \varphi(x)\, \varphi_x(x-k_1) \cdots \varphi_{xx}(x-k_2) \cdots dx.$$

We have found *exact* methods for evaluating the functionals required in the wavelet–Galerkin method. A typical functional would be the three-term *connection coefficient*

$$\Omega(k, j) = \int \varphi_{xx}(x)\, \varphi_x(x-k)\, \varphi(x-j)\, dx.$$

Since the scaling function used to define compact wavelets has a limited number of derivatives, the numerical evaluation of these expressions is often unstable or inaccurate.

The exact method is based on use of the *scaling relation*

$$\varphi(x) = \sum_{k=0}^{N-1} a_k \varphi(2x-k).$$

By the obvious manipulations a system of equations is found for the $\Omega(k, j)$. The system of equations is generally rank deficient (singular). The rank deficiency is cured and a unique solution is obtained by the inclusion of an additional set of linear equations that are obtained from the *moment* equations. The resulting system is non-singular and non-homogeneous and has a unique solution that is easily found by standard techniques. This technique is derived in the recent paper by Latto, Resnikoff, and Tenenbaum [9].

We remark that some of the three-term connection coefficients have magnitudes of the order of $1.e-14$. As will be shown later, the smaller values contribute in an essential way to the accuracy of the evaluation of the nonlinearities in the Navier–Stokes equations.

Our original expansion is over the *space* dependence of the solution. If the equation has a time dependence the resulting equations for the $\hat{U}_k$ will be a system of ordinary differential equations in t.

See Fig. 2 from [10] for examples of Burgers shock capture at a Reynolds number of 2000, using the wavelet–

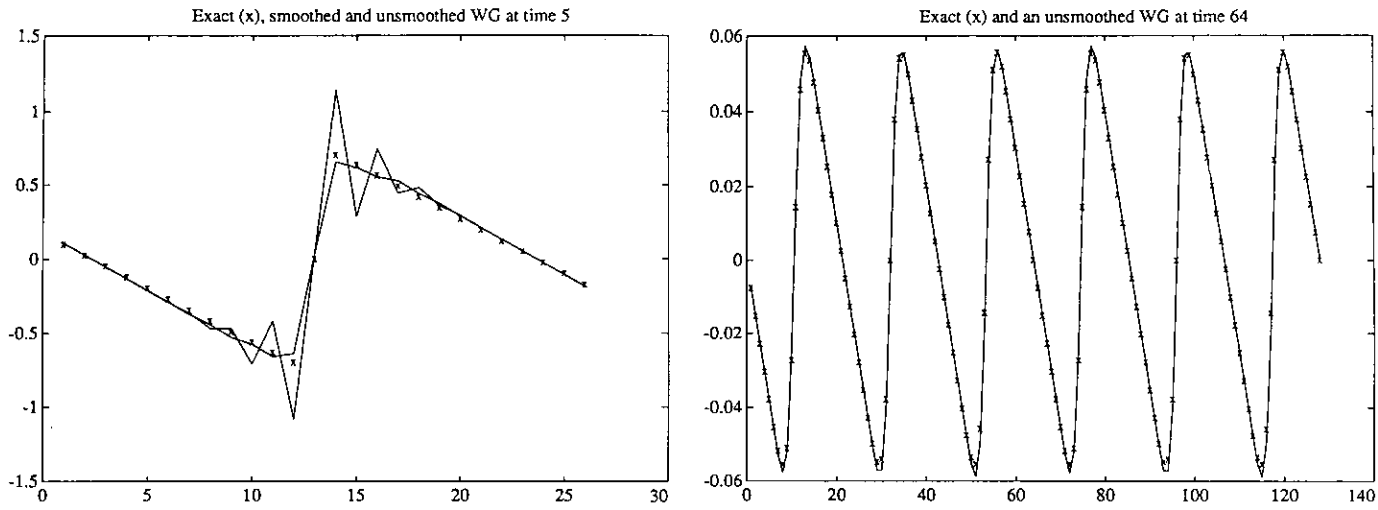

FIG. 2. Comparison of exact (x) solution and wavelet–Galerkin approximation: on the left, smoothed and exact at time 5; on the right unsmoothed and exact at time 64.

Galerkin method. The simple three-point smoothing of the approximate solution is nearly exact and for large time the approximation is nearly exact without smoothing.

We have defined the approximation of the solution in the wavelet–Galerkin method by translates of the scaling function. It is also possible to define the approximation of the solution by translates of the scaling function and associated wavelet terms. It might be thought that the scaling function–wavelet expansions could produce different numerical results. In Fig. 3 we show superimposed the results for solving the Burgers equation with scaling function and scaling function–wavelet translates. The results are not distinguishable in this figure. Figure 4 shows the difference of the solution produced by the two expansions. In general, to a tolerance the methods are identical.

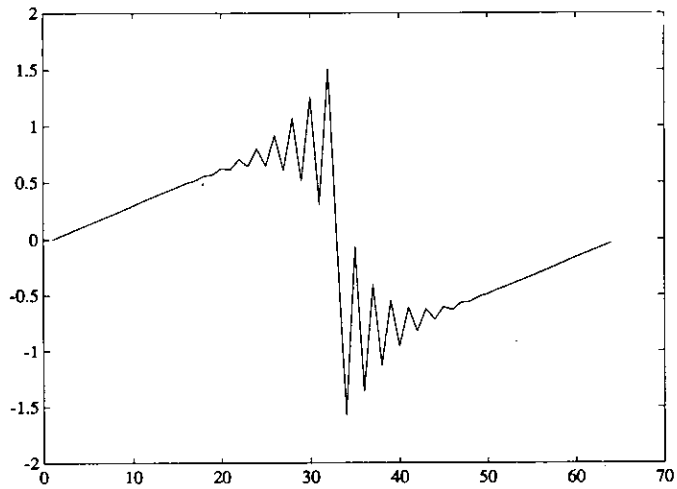

FIG. 3. Comparison of scaling function and scaling function–wavelet expansions for Burgers equation.

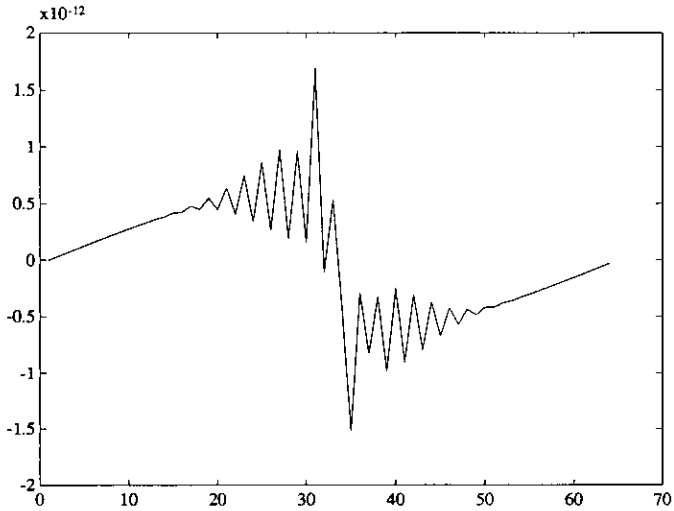

FIG. 4. Difference of scaling function and scaling function–wavelet expansions for Burgers equation.

2.3. *The Two-Dimensional Navier-Stokes Equation*

The two-dimensional Navier–Stokes equations in the stream function–vorticity formulation are

$$c_t + \psi_y c_x - \psi_x c_y = \sigma\, \Delta c$$
$$\Delta \psi = -c.$$

The velocity field is $u = \psi_y$ and $v = -\psi_x$.

In applying the wavelet–Galerkin method to the two-dimensional Navier–Stokes equation in the stream function–vorticity formulation

$$c_t + \psi_y c_x - \psi_x c_y = \sigma\, \Delta c$$
$$\Delta \psi = -c,$$

we expand and approximate the stream function and vorticity in terms of the scaling function φ [16]:

$$\psi(x, y) = \sum_{j=1}^{N} \sum_{k=1}^{N} \Psi_{j,k} \varphi(x-j)\, \varphi(y-k),$$

$$c(x, y) = \sum_{j=1}^{N} \sum_{k=1}^{N} C_{j,k} \varphi(x-j)\, \varphi(y-k).$$

Since we assume periodic boundary conditions there is a periodic wrap around in (x, y) and we let the period scale with the number of terms in the expansion. This allows neglect of the dilation factor in the scaling function. Substituting into the equation and projecting the result onto the subspace spanned by $\{\varphi(x-j)\, \varphi(y-k)\colon j=1, \ldots, N;\ k=1, \ldots, N\}$ requires evaluating terms of the form

$$\int \varphi_{xx}(x)\, \varphi_x(x-j)\, \varphi(x-k)\, dx.$$

This uniquely determines the $\Psi_{j,k}$ and $C_{j,k}$ as solutions of the wavelet–Galerkin ordinary differential equations.

Define the *connection coefficients*

$$\Omega_j^{02} = \int \varphi(x)\, \varphi_{xx}(x-j)\, dx$$

$$\Omega_{jl}^{100} = \int \varphi_x(x)\, \varphi(x-j)\, \varphi(x-l)\, dx$$

$$\Omega_{km}^{001} = \int \varphi(x)\, \varphi(x-k)\, \varphi_x(x-m)\, dx.$$

With the summation convention on the indices (p, q, j, l, k, m) the wavelet–Galerkin equations are

$$C_t(p, q) + C(j+p, k+q)\, \Psi(l+p, m+q) \times (\Omega_{j,l}^{100} \Omega_{k,m}^{001} - \Omega_{j,l}^{001} \Omega_{k,m}^{100}) = \sigma(\Omega_j^{02} C(j+p, q) + \Omega_k^{02} C(p, k+q))$$

and

$$C(p, q) = -\Omega_j^{02} \Psi(j+p, q) - \Omega_k^{02} \Psi(p, k+q).$$

The Jacobian. The wavelet–Galerkin expansion of the nonlinear, Jacobian term Θ can be expressed in a compact form [16]. Let $\hat{C}$ and $\hat{\Psi}$ be the matrices of coefficients for the vorticity and the stream function. Let Ω and J be the (m, m) matrices of coefficients that depend on the wavelet basis. In our case, these are Ω^{100} and Ω^{001}. Let $\hat{C}(p, q)$ and $\hat{\Psi}(p, q)$ be, with periodic wrap around, the (m, m) matrices with entries from $\hat{C}$ and $\hat{\Psi}$ centered on the (p, q) element. Then the evaluation of the (p, q) element is of the form

$$\Theta(p, q) = \sum_{j=1}^{m} \sum_{k=1}^{N} H(p, q)_{j,k},$$

where

$$\hat{H}(p, q) = \Omega \hat{C}(p, q) \cdot^* \hat{\Psi}(p, q)\, J - J \hat{C}(p, q) \cdot^* \hat{\Psi}(p, q)\, \Omega$$

and $\cdot^*$ is the term by term product for matrices.

The wavelet–Galerkin operator Θ depends on the vorticity and stream function fields and is a conservative approximation to the Jacobian of these fields. It can be easily shown, using the orthogonality of the translates of the scaling function and the properties of the Jacobian operator that,

$$\sum_p \sum_q C(p, q)\, \Theta(p, q) = 0$$

$$\sum_p \sum_q \Psi(p, q)\, \Theta(p, q) = 0.$$

These relations directly imply that the wavelet–Galerkin approximation of the Jacobian will conserve both vorticity and energy.

In comparison to the additional required operations, the speed of evaluation of the nonlinear Jacobian terms for these equations determines the speed of execution of this algorithm. Therefore, we seek to minimize the floating point operations required to evaluate these terms.

The unoptimized evaluation of these expressions requires

$$(4m^3 + 3m^2)\, N^2$$

floating point operations for a complete evaluation of the nonlinear terms.

We have found an initial optimization (fast algorithm) that calculates the complete nonlinear interaction in

$$15m^2N^2 + 10m^3N + 3m + 2N$$

floating point operations. This fast algorithm is based on a simple recursion relation relating $\hat{H}(p, q)$ to $\hat{H}(p-1, q)$ and $\hat{H}(p, q-1)$.

The initial optimization is based on the following observation. If we know $\Omega \hat{C}(p, q)$ then

$$\Omega \hat{C}(p, q+1) = \Omega \{\hat{C}(p, q)\, \hat{D} + \hat{S}(p, q+1)\}.$$

$\hat{D}$ is the matrix that shifts the columns to the left by one column and assigns the null column to last one and

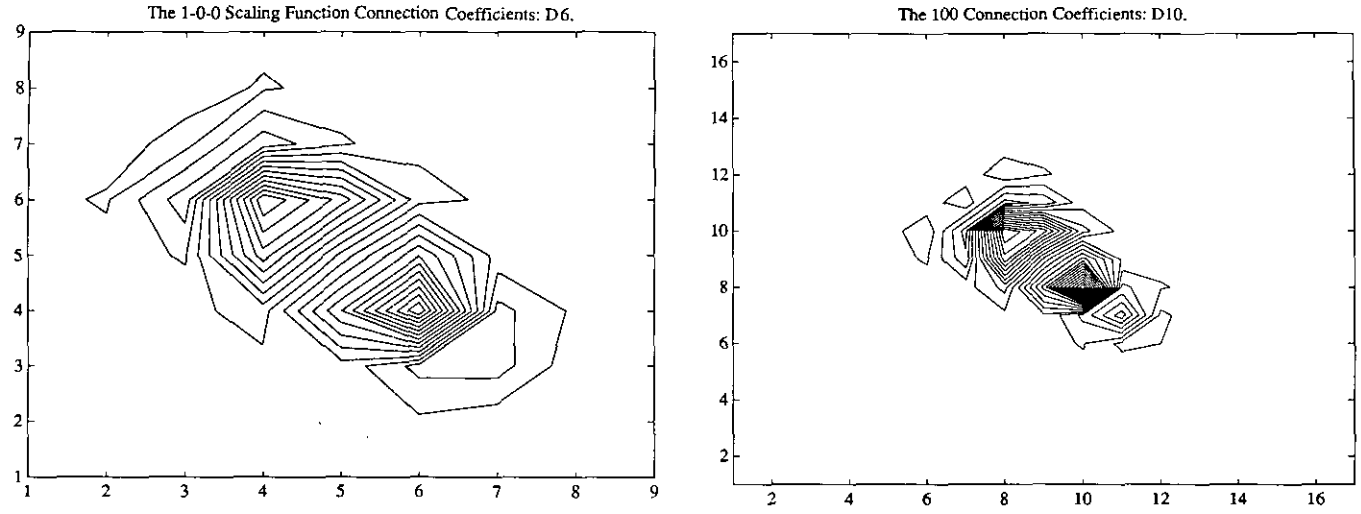

FIG. 5. The 100 $D6$ and $D10$ scaling function connection coefficients.

$\hat{S}(p, q+1)$ is the matrix with null columns except the last one which is the last column of $\hat{C}(p, q+1)$. This process reduces the evaluation of $\Omega\hat{C}(p, q+1)$ to shifts and one matrix–vector multiplication. Using symmetries of Ω and the form of the nonlinearity the operations count can be further reduced.

Beyond the evaluation of each nonlinear term, the number of nonlinear terms to evaluate depends on the form of the equation under consideration. For instance, the stream function form of the 2D Euler equation requires the evaluation of a factor of three more nonlinear terms than the vorticity form of the 2D Euler equation. For this reason it is important to consider optimizations with respect to the equation formulation and wavelet basis. This optimization should consider both the speed of execution and the accuracy of the result.

For the Daubechies six-term scaling function ($D6$), $m = 9$ and the vorticity formulation requires 5,443,355 operations when $N = 64$. For $D8$, $m = 13$, and $N = 64$, the vorticity formulation requires 11,789,607 operations. For comparison the de-aliased FFT evaluation requires 5,881,935 operations when $N = 64$. Thus, the wavelet vorticity based algorithm with $D6$, as currently developed, is faster than the dealiased FFT algorithm (that uses shifted grids to eliminate aliasing terms) [3].

In the operation count given above the most important term is $15m^2N^2$. Of this $4m^2N^2$ operations are required for initializations and is irreducible; $11m^2N^2$ operations are required to complete the evaluations and these arise from the product of connection coefficient matrices Ω and a data vector $\hat{v}$, $\Omega\hat{v}$. However, approximately 40% of the entries of Ω are null.

Figure 5 shows a contour plot of the connection coefficient matrix Ω^{100} for the six- and ten-term Daubechies scaling functions. There are many terms with nonzero yet small magnitude. The smallest nonzero terms in the ten-term case have magnitudes of the order $1.e-15$.

By not multiplying the components of Ω that are null the $11m^2N^2$ operations can be reduced to approximately $7m^2N^2$ operations. We have implemented this procedure.

It might seem that, given the magnitude of some of the terms in Ω^{100}, a considerable further improvement in the reduction of operations could be achieved by not multiplying terms whose connection coefficients are smaller than a prescribed tolerance. To investigate this, we have filtered the connection coefficients to a prescribed tolerance and found the effect of this on the accuracy of the evaluation of the Jacobian nonlinearity. The results are shown in Table I. In general this procedure does not seem to be warranted.

TABLE I

The Effects of Filtering Connection Coefficients on the Accuracy of the Jacobian Nonlinearity Evaluated Using D10

Tol	Max. error	Number of terms
$1.e-20$	$1.2173e-13$	217
$1.e-16$	$1.2173e-13$	217
$1.e-15$	1.2173e-13	214
1.e-14	2.1079e-12	212
1.e-13	1.5502e-12	208
1.e-12	1.9641e-11	202
1.e-11	1.1209e-8	182
1.e-10	1.3423e-8	173
1.e-9	3.5131e-8	159
1.e-8	1.1877e-6	149
1.e-7	1.5887e-5	130
1.e-6	1.9740e-4	117
1.e-5	1.8000e-3	92
1.e-3	2.9560e-1	51

Note. There are 217 nonzero coefficients.

The Laplacian. The relationship of the vorticity and stream function fields is described by the following matrix equation [16]

$$C = -\Omega\Psi - \Psi\Omega,$$

where Ω is a circulant matrix whose rows are periodically shifted copies of the two-term connection coefficient vector Ω^{02}

$$\Omega = \text{circ}\{\Omega_0, \Omega_1, ..., \Omega_p, 0, ..., 0, \Omega_{-p}, ..., \Omega_{-1}\},$$

where

$$\Omega_j = \int \varphi(x)\, \varphi_{xx}(x-j)\, dx.$$

Note that $\Omega = \Omega^t$.

All circulant matrices commute and have a common set of eigenvectors. In effect, Ω can be diagonalized by

$$\Omega = \Phi\, D_\Omega \Phi^t,$$

where $N = 2m$

$$D_\Omega = \text{diag}\{\lambda_j\}$$

$$\lambda_j = \Omega_0 + 2 \sum_{k=1}^{p} \Omega_k \cos\left(\frac{2\pi jk}{N}\right)$$

and

$$\Phi = \frac{\sqrt{2}}{\sqrt{N}} \times \begin{pmatrix} 1/\sqrt{2} & 1 & \cdots & 1 & 1/\sqrt{2} & 0 & \cdots & 0 \\ 1/\sqrt{2} & c_1 & \cdots & c_{m-1} & -1/\sqrt{2} & s_{m-1} & \cdots & s_1 \\ \vdots & \vdots & \cdots & \vdots & \vdots & \vdots & \cdots & \vdots \\ 1/\sqrt{2} & c_{N-1} & \cdots & c_{(m-1)(N-1)} & -1/\sqrt{2} & s_{(m-1)(N-1)} & \cdots & s_{(N-1)} \end{pmatrix},$$

where $c_j = \cos(2\pi j/N)$ and $s_j = \sin(2\pi j/N)$. We note that $\Phi\Phi^t = I$.

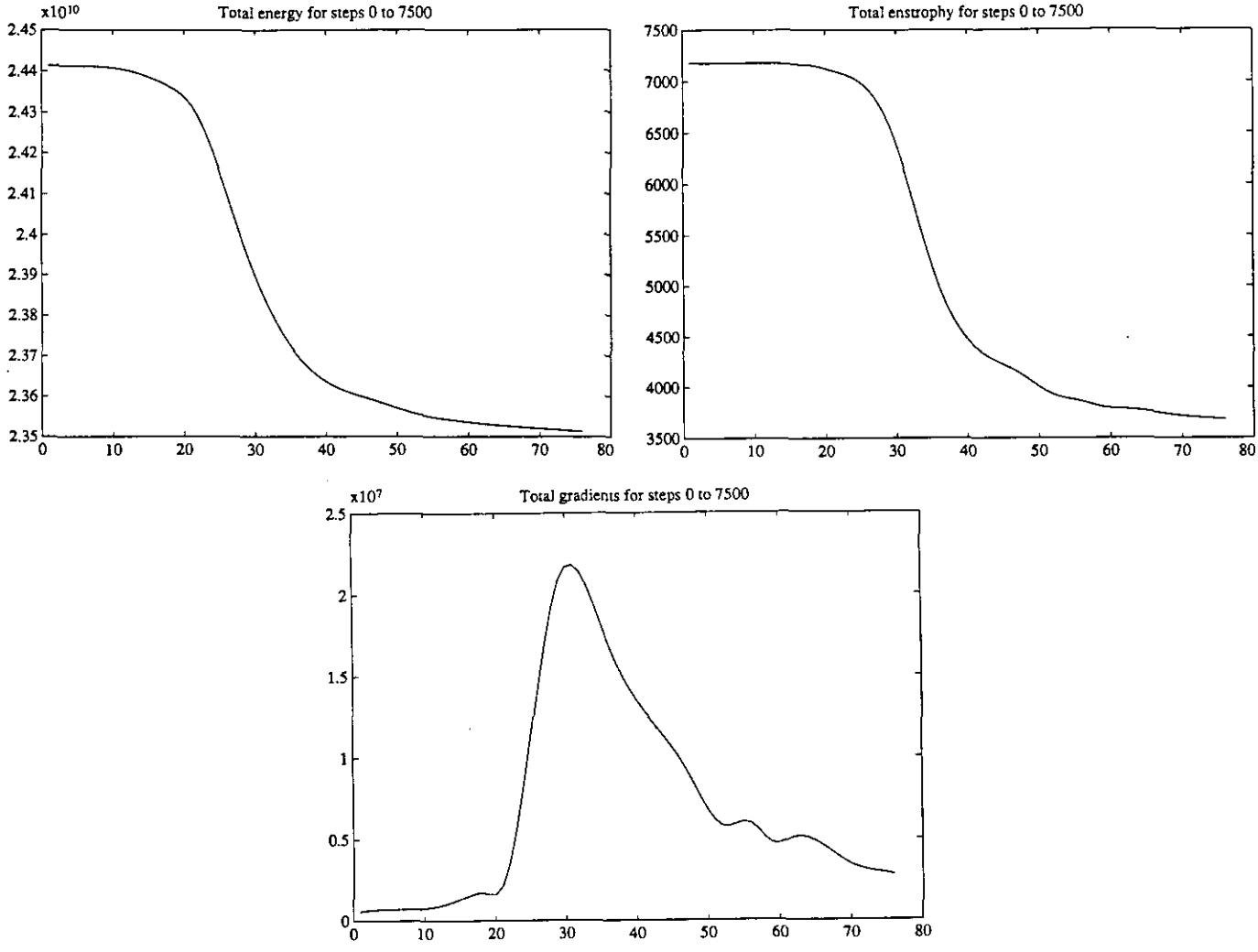

FIG. 6. The evolution of energy, enstrophy, and the gradients of vorticity.

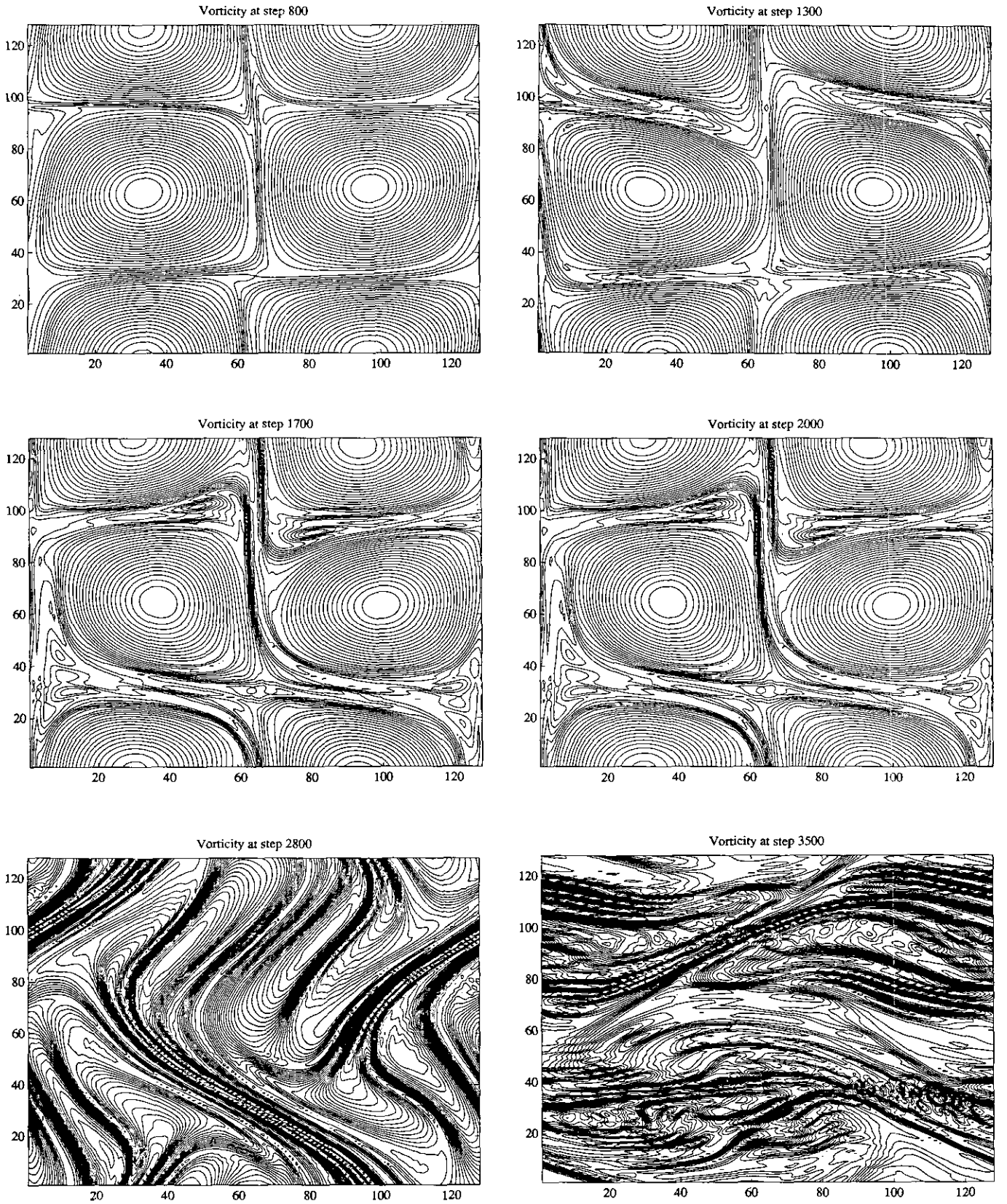

FIG. 7. The evolution of the vorticity, times 800 through 3500.

In terms of the above the wavelet–Galerkin Laplacian is inverted to solve for the stream function Ψ,

$$\Psi = \Phi(B_\Omega .\backslash (\Phi' C \Phi))\, \Phi',$$

where $.\backslash$ is the componentwise division operator and

$$B_\Omega = D_\Omega \begin{pmatrix} 1 & 1 & \cdots & 1 \\ \vdots & \vdots & \cdots & \vdots \\ 1 & 1 & \cdots & 1 \end{pmatrix} + \begin{pmatrix} 1 & 1 & \cdots & 1 \\ \vdots & \vdots & \cdots & \vdots \\ 1 & 1 & \cdots & 1 \end{pmatrix} D_\Omega .$$

This procedure has been implemented using the fast Fourier transform.

Some Numerical Results. We find the wavelet-based algorithms are considerably more stable for high Reynolds number flows. This allows the above iterative implementation of implicit time stepping methods for the Euler flow [16].

As described in [16] we integrate the Euler equations with backward-Euler time differencing

$$(c_{n+1} - c_n)/dt + J(c_{n+1}, \psi_{n+1}) = 0$$
$$\Delta \psi_n = -c_n,$$

and a $D6$ wavelet–Galerkin spatial discretization. The backward-Euler differencing does not conserve the energy or the enstrophy. However, it does strongly damp the high frequency components of the solution. This makes backward-Euler differencing quite useful for inviscid calculations since without the specific inclusion of viscosity it tames the small-scale terms near the resolution cutoff.

At each time step we solved the implicit difference scheme by iteration

$$v_{j+1} = c_n - dt \cdot J(v_j, \Delta^{-1} v_j)$$

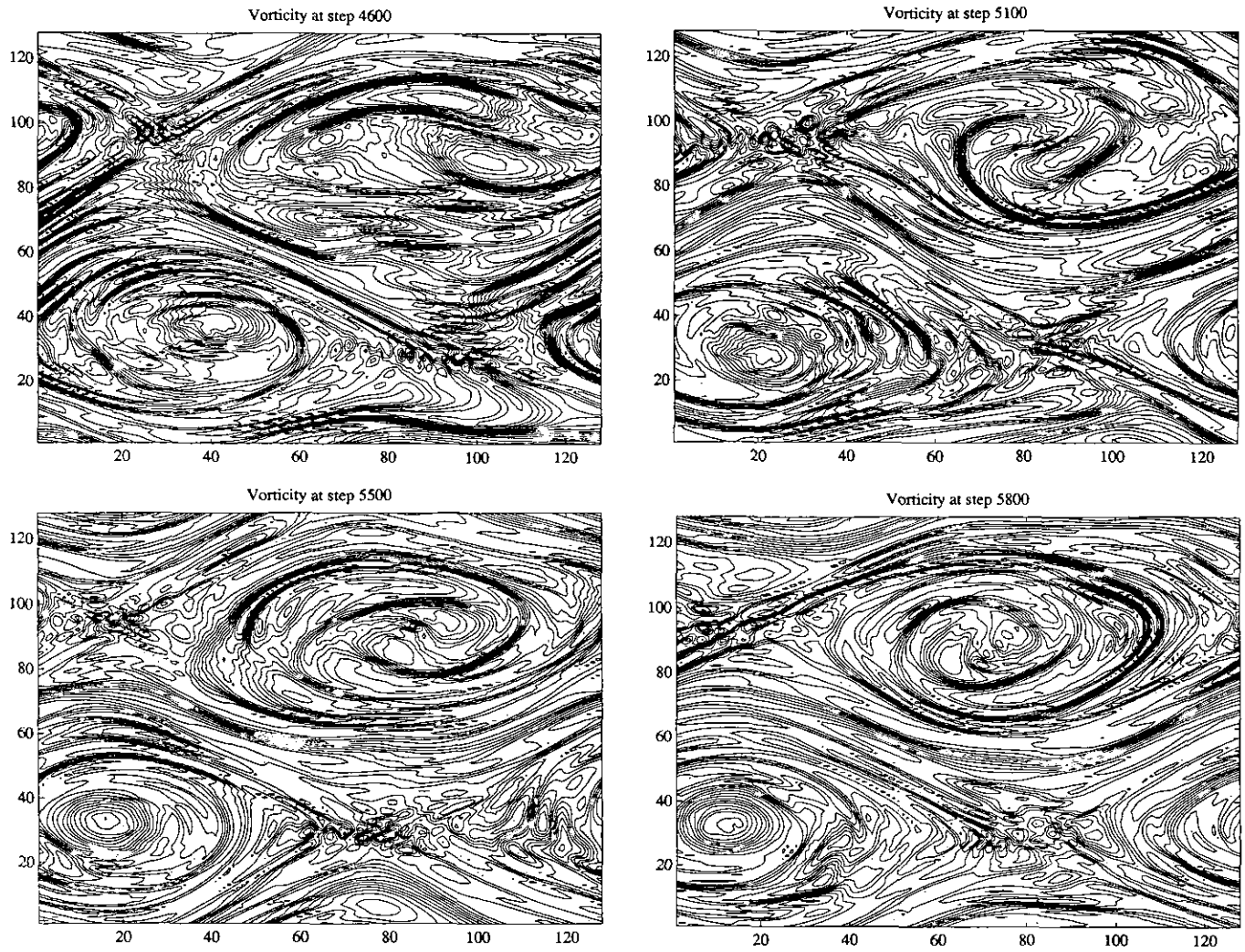

FIG. 8. The evolution of the vorticity, times 4600 through 7500.

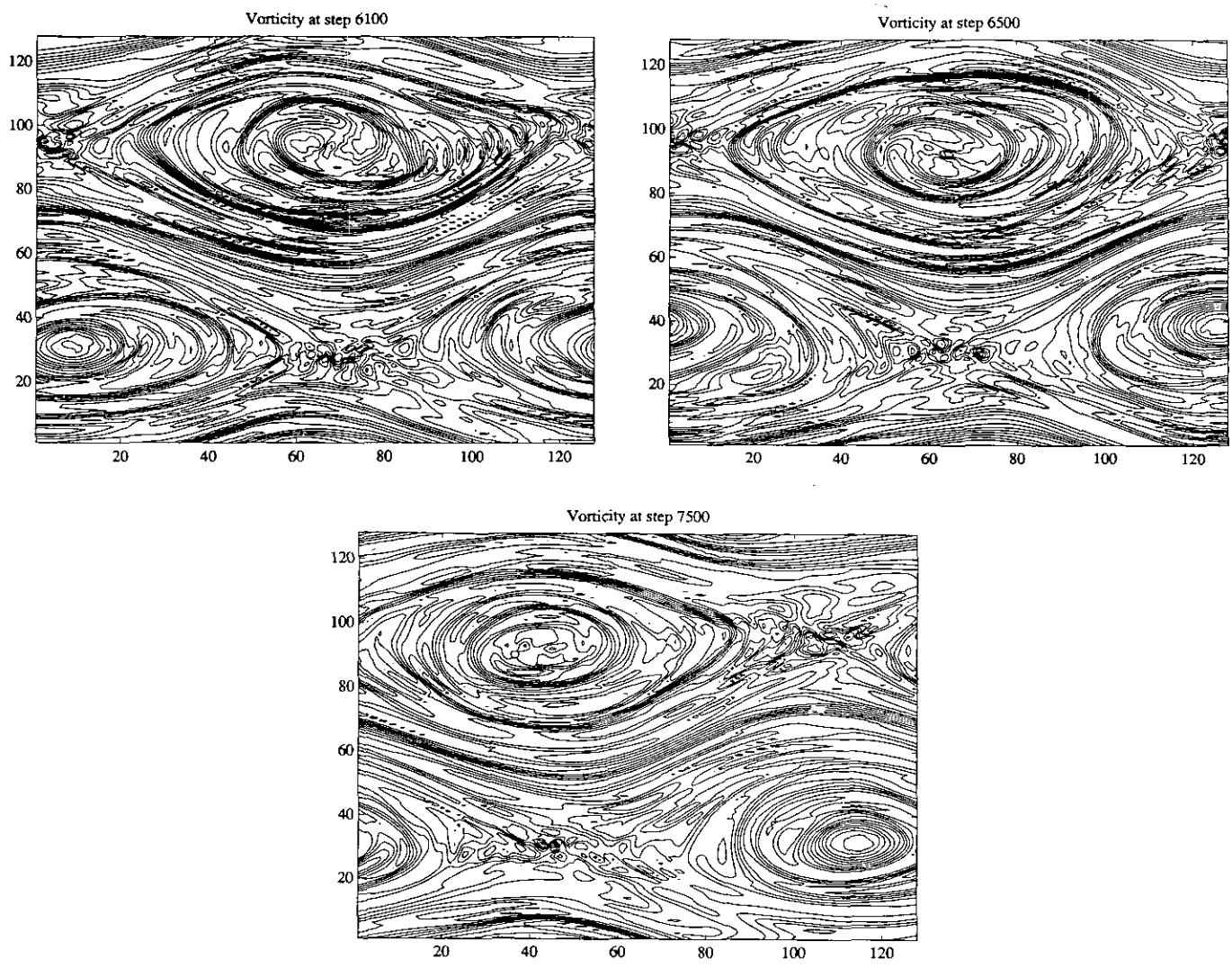

Fig. 8—*Continued*

until

$$\sup |v_{j+1} - v_j| < \varepsilon.$$

In this experiment $\varepsilon = 1.e-3$, $dt = 0.025$, and the maximum initial vorticity has a magnitude of 1.4017.

We integrated the equations for 7500 time steps of magnitude 0.025. In this period of time the solution undergoes a sharp transition from an unstable steady state toward, to what appears to be, a stable, steady state solution. During this period of time the algorithm approximately conserves energy while transferring about one-half of the enstrophy out of the solution. The related gradients of vorticity are largest just before the event transferring the vorticity occurs.

Figure 6 shows the evolution of energy, the evolution of enstrophy, and the evolution of the gradients of vorticity.

Figures 7 and 8 show the evolution of the vorticity field. We show a field produced by a three-point smoothing in the x and then the y directions. Even though the numerical solution has a considerable oscillatory component, the tensor product three-point smoothing produces a consistent and smooth result.

2.4. *The Periodic Helmholtz Equation*

Before considering the Helmholtz equation in non-separable geometry, we examine the degree of approximation of the wavelet–Galerkin method applied to the periodic problem (the Helmholtz equation on a torus),

$$(-\Delta + \alpha)\, U = F.$$

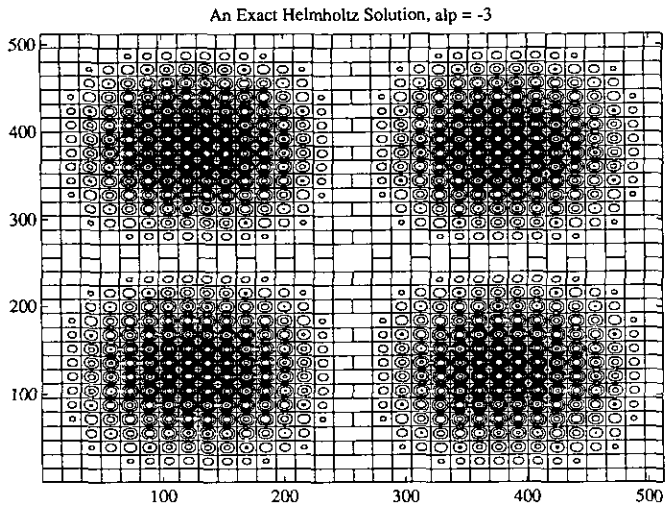

FIG. 9. The exact solution of the periodic Helmholtz equation with $\alpha = -3$.

We specify an exact solution U and apply the Helmholtz operator to find F. We then use the discretization of F with a five-point finite difference and wavelet–Galerkin periodic solvers to find a set of approximate solutions that can be compared to the exact solution in the sup norm. The discretizations are of size 64, 128, 256, and 512. The wavelet–Galerkin bases are $D6$, $D8$, $D10$, $D12$, $D14$, $D16$, $D18$, and $D20$. The parameter $\alpha = -3$ and the period is of length 1.

Figure 9 shows the exact solution. Figure 10 shows the natural log of the sup norm error and the slope of the log of the error to base two. Note that the slopes for $D12$ through $D20$ are affected by the double precision round off error. Since we double the resolution with each sample the second plot in Fig. 10 implies that the sup norm of the error for basis DN vanishes as

$$(\delta x)^N.$$

The rate of decay of error with discretization is faster than that which might be expected from the results of Section 2.1. These assert that the error of approximation in a basis DN for a function with at least $N/2$ derivatives will decay as

$$(\delta x)^{N/2}.$$

Therefore, the periodic wavelet–Galerkin solver produces a solution with double the expected rate of convergence. We will compare this with the rate of convergence for the capacitance matrix implementation presented in the next section.

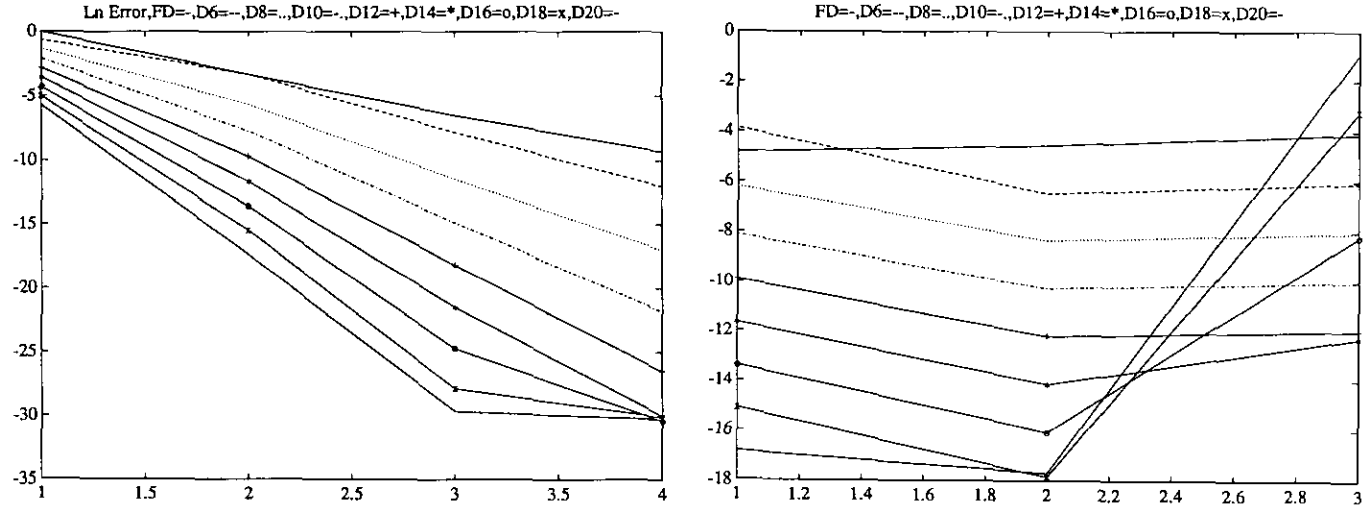

FIG. 10. The natural log of the sup norm error and the slope of the log (base 2) of the sup norm error.

3. THE WAVELET–CAPACITANCE MATRIX METHOD

We will describe the method for the harmonic Helmholtz equation

$$(-\Delta+\alpha)\,U=F$$

in a domain D with boundary conditions $U=g$ on the boundary of D. One version of the direct method is equivalent to a numerical implementation of the single layer potential [14]. A method based on the double layer potential is also a possibility [13]. The algorithm is based on the calculation of a numerical *partial Green's Function* [14].

The outline of our method is as follows. Regard the domain D as contained (embedded) in a periodic cell, S. We extend F from D to S in a smooth way. The extension $\hat{F}$ is periodic on S. We also define a periodic function $\hat{\rho}$, where $\hat{\rho}$ is zero except on the support of $\partial D \subset S$. We determine $\hat{\rho}$ so that the periodic solution in S,

$$(-\Delta+\alpha)\,U=\hat{F}+\hat{\rho},$$

will verify the boundary conditions $U=g$ on ∂D. By construction the equation $(-\Delta+\alpha)\,U=F$ is satisfied in D.

One advantage of this method is the use of fast and accurate periodic solvers to evaluate the solution. Another advantage is the efficient inclusion of general non-separable geometries without special case treatments. A possible disadvantage is the use of functions that are singularly supported in S. This can lower the accuracy of the numerical solution through Gibbs' phenomena and boundary residual errors.

We have extended the method by allowing the support of $\hat{\rho}$ to be separate from the boundary of D, ∂D. When the equations are discretized by the wavelet–Galerkin method, this extension eliminates the boundary residuals and defines a spectrally accurate method for non-separable domains. To our knowledge this algorithm is the first implementation of its type. We will present an extensive series of numerical calculations that support our conclusions about accuracy and convergence.

The numerical implementation is straightforward. In effect, we expand the solution in periodic, wavelet–Galerkin basis

$$U=\sum\sum U_{i,j}\varphi(x-i)\,\varphi(y-j),$$

where φ is a scaling function. To calculate the Green's function we resolve the delta function in the space of translates of scaling function

$$\lambda_{x_0,y_0}(x,y)=\sum\sum \varphi(x_0-i)\,\varphi(x-i)\,\varphi(y_0-j)\,\varphi(y-j).$$

Since the translates of the scaling function are orthogonal and complete in L^2, the above expression implies that for the Galerkin approximation, $\tilde{f}$, of a square integrable function, f,

$$\tilde{f}(x_0,y_0)=\iint dx\,dy\,\lambda_{x_0,y_0}(x,y)\,\tilde{f}(x,y),$$

which is the definition of the delta function in this subspace.

Therefore, we solve, by the wavelet–Galerkin method [16], the equation

$$(-\Delta+\alpha)\,G(x,x_0;y,y_0)=\lambda_{x_0,y_0}(x,y)$$

for the partial Green's function, G. To find the usual capacitance matrix, C, we discretize the boundary into a series of points $\hat{x}_j$ and form the matrix whose (i,j) component is $G(\hat{x}_i,\hat{x}_j)$. The evaluation of G requires only one solution of the periodic, fast, wavelet–Galerkin solver [13].

In our formulation of the algorithm, we discretize the boundary by the points $\hat{x}_j$ and the support of $\hat{\rho}$ in S by the points $\hat{y}_j$. The definition of the capacitance matrix is then

$$C_{i,j}=G(\hat{x}_i,\hat{y}_j).$$

Depending on the cardinality of the sets $\hat{x}$ and $\hat{y}$, the system of equations for the discrete potential $\hat{\rho}$ are determined, overdetermined, or underdetermined. We have examined these possibilities and will present the results in this paper. In general, if $\hat{y}$ is exterior to $\hat{x}$, we obtain excellent numerical results that depend stably on the choice of $\hat{y}$.

In terms of the (extended) capacitance matrix, the discrete potential of a single layer is a solution of the system

$$\hat{g}=C\hat{\rho}.$$

For non-determined systems we use a singular value decomposition of C to find the least square or minimal norm solution [7].

For a specified geometry the capacitance matrix can be *inverted* once and for all and when $\hat{\rho}$ is extended from the discrete support to the periodic domain (equal to zero at non-support points), the solution of the Helmholtz equation with boundary data g is found by one fast, periodic wavelet–Galerkin solution. As described in [13, 14] the general inhomogeneous case reduces to this homogeneous problem.

The primary advantage of the direct method in comparison to the iterative methods is that the (discrete) boundary conditions are satisfied identically, and the method works near the *resonance* cases encountered in the solution of the Helmholtz equation. For domains that require many points for their discretization, the direct method could become impractical. We suggest that in these

cases a fairly sparse selection of source points $\hat{y}$ in the direct method can effectively *initialize* an iterative (conjugate-gradient) method (even near resonance).

4. NUMERICAL RESULTS FOR THE HELMHOLTZ EQUATION

In this section we have examined the numerical solution of the Helmholtz equation

$$(-\Delta + \alpha)\, U = F$$

in an L-shaped two-dimensional domain. The domain has sides of length 64. We examine solutions with $\alpha = -3, 0, 0.3, 3$. Normalized to a side of length 1, $\alpha = -12288$, 0, 1228.8, 12288. In terms of the spectrum of the discrete problem, these are mid to high frequency solutions. The boundary data is proportional to $\sin(2\pi x)$ and $\sin(4\pi x)$. The domain and boundary data are shown in Fig. 11.

We have also examined solutions in domains that are rectangles, triangles, and combinations of both. The results closely parallel those for the L-shaped region. In fact, for domains of similar area, we have found that the rates of convergence appear to be independent of the shape. Therefore, the results for the L-shape region apply to a diverse collection of regions.

The primary factor that controls the rate of convergence is the numerical resolution of the singular function $\hat{\rho}$.

Therefore, to examine the convergence it is enough to assume that the smooth function $\hat{F} = 0$.

The term $N128D16$ will indicate a solution with a discretization with $N = 128$ and basis $D16$. The term $N128FD$ indicates a solution with discretization 128 found using finite differences.

We place the support of $\hat{\rho}$ at a distance from the boundary that is equal to the support of the basic scaling function. Therefore, the offset for $N128D16$ is equal to 15 units exterior to the boundary.

Except where noted, the discrete residual and boundary errors for the wavelet method in $D \cup \partial D$ are found to be small to the order of double precision roundoff error, 1.e − 12.

Again, we use the pointwise sup norm (not the L^2 norm) to measure the error in this paper. The L^2 norms are quite smaller. However, the sup norm provides a better measure of the error and related convergence.

4.1. *The Hyperbolic, or Indefinite, Case*: $\alpha = -12288$

We consider discretizations of size $N = 64$, 128, 256, 512 and scaling functions corresponding to the 16, 20, 24, 28, and 32 Daubechies scaling functions. That is, $D16$, $D20$, $D24$, $D28$, and $D32$. Figure 12 shows the contour and mesh plots of the solution with boundary data proportional to $\sin(2\pi x)$. Figure 13 shows the contour and mesh plots of the solution with boundary data proportional to $\sin(4\pi x)$.

Spectral convergence, $N = 64$. The boundary data is proportional to $\sin(2\pi x)$. For this problem the $N = 64$ discretization is coarse. We consider the solution for several scaling function bases. The data is as follows:

- $\|N64D20 - N64D16\| = 0.2514$;
- $\|N64D24 - N64D20\| = 0.0815$;
- $\|N64D28 - N64D24\| = 0.0256$;
- $\|N64D32 - N64D28\| = 0.00799$.

The ratio of the above numbers indicates the rate of convergence. We find that:

- $\|N64D20 - N64D16\| / \|N64D24 - N64D20\| = 3.0861$;
- $\|N64D24 - N64D20\| / \|N64D28 - N64D24\| = 3.1772$;
- $\|N64D28 - N64D24\| / \|N64D32 - N64D28\| = 3.2084$.

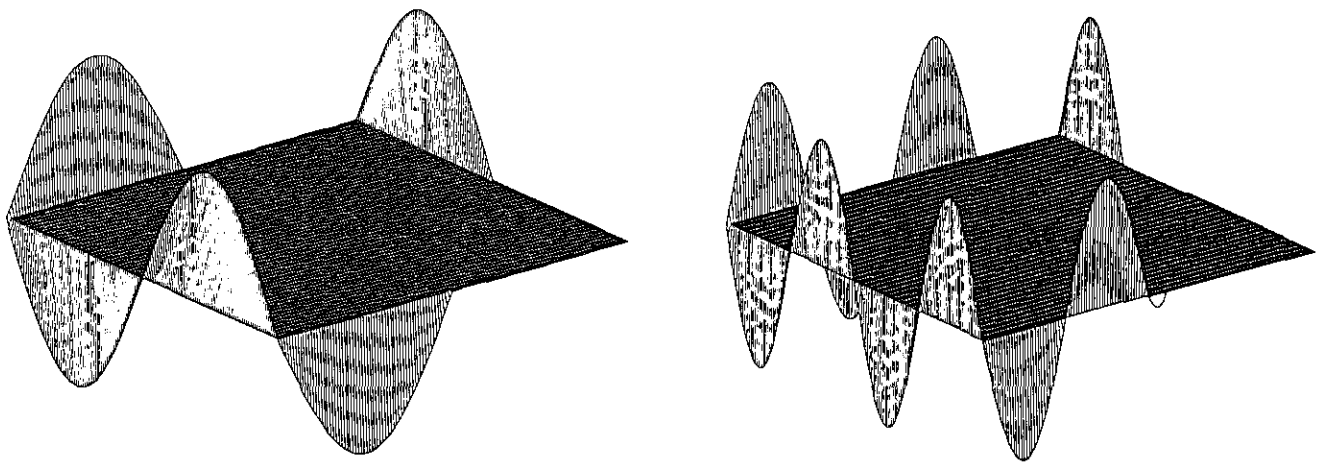

FIG. 11. The domain and boundary data for the numerical solutions of the Helmholtz equation.

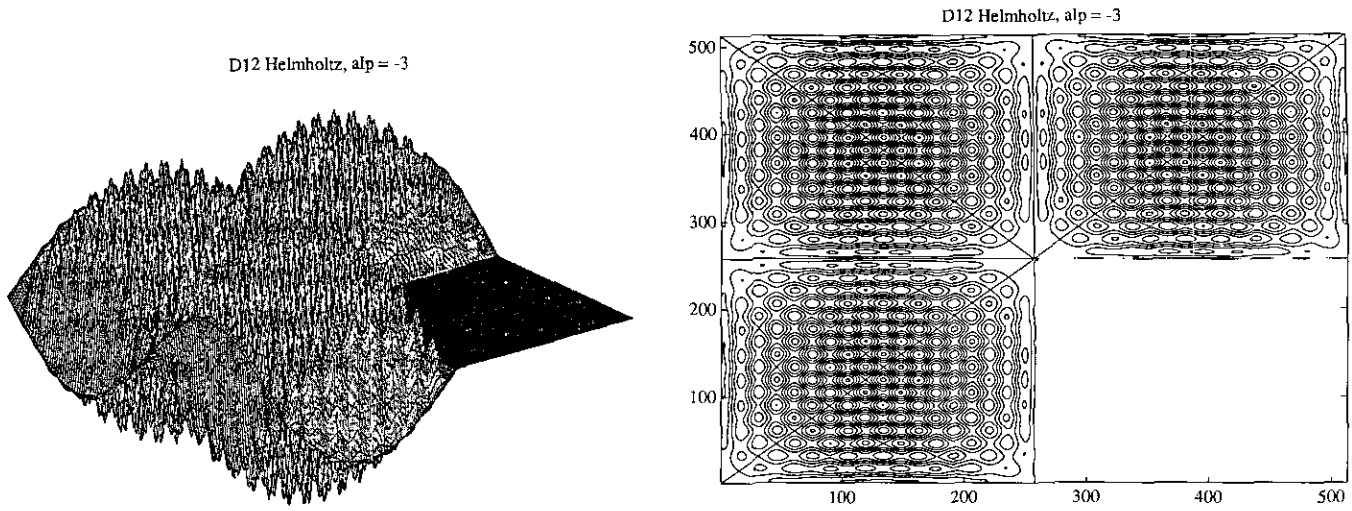

FIG. 12. The contour and mesh plots of the Helmholtz solution with boundary data proportional to $\sin(2\pi x)$ and $\alpha = -3$.

Therefore, we see spectral convergence at a fairly constant rate for a low level of discretization.

Spectral convergence, $N = 128$. The discretization $N = 128$ is well resolved for higher order scaling functions and shows a spectral convergence as the order of the basis function is increased. The boundary data is proportional to $\sin(4\pi x)$. The data is as follows:

- $\|N128D16 - N128D12\| = 6.22902e-3$;
- $\|N128D20 - N128D16\| = 1.5796e-4$;
- $\|N128D24 - N128D20\| = 4.1692e-6$;
- $\|N128D28 - N128D24\| = 1.19566e-7$.

The ratio of the above numbers indicates the rate of convergence. We find that:

- $\|N128D16 - N128D12\|/\|N128D20 - N128D16\| = 39.4$;
- $\|N128D20 - N128D16\|/\|N128D24 - N128D20\| = 37.88$;
- $\|N128D24 - N128D20\|/\|N128D28 - N128D24\| = 34.87$.

The boundary data is proportional to $\sin(2\pi x)$. The data is as follows:

- $\|N128D16 - N128D12\| = 6.13511e-3$;
- $\|N128D20 - N128D16\| = 1.58837e-4$;
- $\|N128D24 - N128D20\| = 4.27067e-6$;
- $\|N128D28 - N128D24\| = 1.24096e-7$.

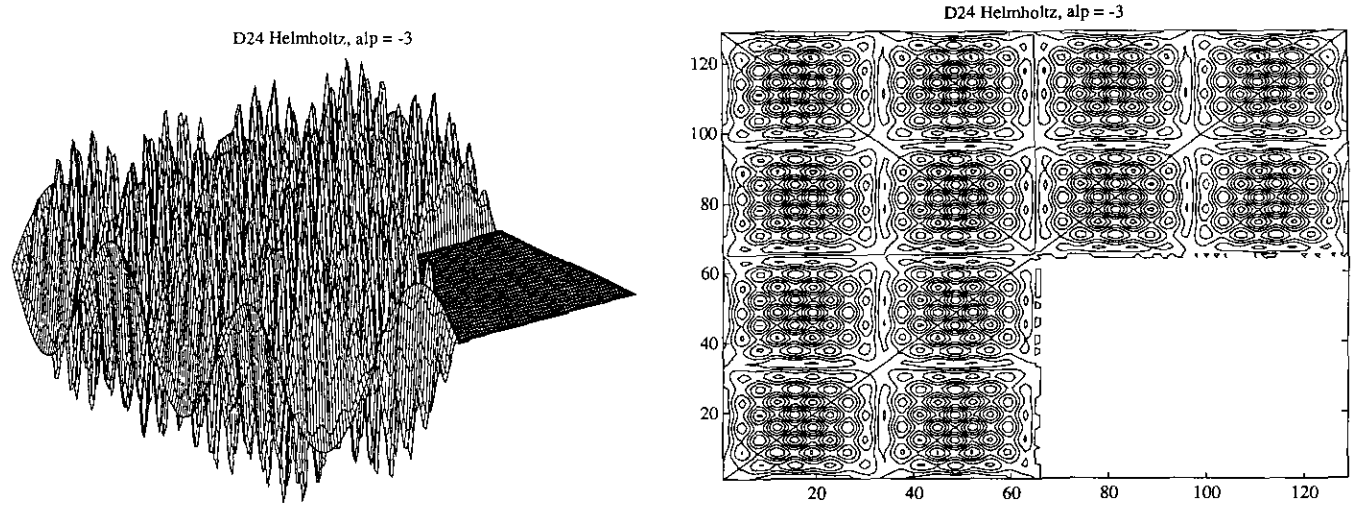

FIG. 13. The contour and mesh plots of the Helmholtz solution with boundary data proportional to $\sin(4\pi x)$ and $\alpha = -3$.

The ratio of the above numbers indicates the rate of convergence. We find that:

- 38.62;
- 37.19;
- 34.41.

Therefore, we see spectral convergence at a fairly large constant rate for a moderate level of discretization.

Spectral convergence, $N = 256$. The boundary data is proportional to $\sin(2\pi x)$. The discretization $N = 256$ is well resolved for most scaling functions and shows a rapid spectral convergence as the order of the basis function is increased. The data is as follows:

- $\|N256D12 - N256D8\| \approx 0.0058$;
- $\|N256D16 - N256D12\| = 1.0369e - 4$;
- $\|N256D20 - N256D16\| = 6.4439e - 8$;
- $\|N256D24 - N256D20\| = 3.6178e - 8$.

The ratio of the above numbers indicates the rate of convergence. We find that:

- $\|N256D12 - N256D8\|/\|N256D16 - N256D12\| = 55.8741$;
- $\|N256D16 - N256D12\|/\|N256D20 - N256D16\| = 1.609e + 3$;
- $\|N256D20 - N256D16\|/\|N256D24 - N2567D20\| = 1.7811$.

Therefore, we see that the rate of spectral convergence increases with the level of discretization.

Convergence with discretization. The boundary data is proportional to $\sin(2\pi x)$. We examine the convergence while increasing the discretization from 128 to 256 to 512 and keeping the $D12$ basis fixed. The results are:

- $\|N256D12 - N128D12\| = 0.006294$;
- $\|N512D12 - N256D12\| = 1.03564e - 4$.

The factor of convergence is

$$\|N256D12 - N128D12\|/\|N512D12 - N256D12\| = 60.76.$$

We examine the convergence while increasing the discretization from 128 to 256 to 512 and keeping the $D16$ basis fixed. The results are:

- $\|N256D16 - N128D16\| = 1.6322e - 4$;
- $\|N512D16 - N256D16\| = 4.72282e - 8$.

The factor of convergence is

$$3456.1.$$

We examine the convergence while increasing the discretization from 128 to 256 to 512 and keeping the $D20$ basis fixed. The results are:

- $\|N256D20 - N128D20\| = 4.42611e - 6$;
- $\|N512D20 - N256D20\| = 3.68687e - 8$.

The factor of convergence is

$$120.05.$$

The lower factor of convergence is a consequence of the near convergence of the solutions with basis $D20$ and discretization 256. We note that

$$\|N512D20 - N512D16\| = 1.81344e - 8.$$

We compare the higher level of discretization with the lower level of discretization and higher scaling function basis. The data is as follows:

- $\|N128D16 - N256D12\| = 1.5611e - 4$;
- $\|N128D16 - N512D12\| = 1.6306e - 4$;
- $\|N128D20 - N256D12\| = 2.1044e - 5$;
- $\|N128D20 - N512D12\| = 4.4783e - 6$;
- $\|N64D32 - N512D12\| = 0.00365$;
- $\|N256D16 - N512D12\| = 6.1162e - 7$;
- $\|N256D20 - N256D16\| = 6.4438e - 8$.

The above demonstrates the consistency of the various approximations and rates of convergence. Generally, it is much less expensive to increase the order of the scaling function than to increase the order of the discretization.

Empirically, the various rates of convergence for basis DN are approximately proportional to

$$(\delta x)^{N-5}.$$

Convergence with finite difference methods. We examine the convergence of the standard five-point finite difference implementation of the capacitance matrix method. This algorithm is described in detail in Vallis *et al.* [14]. The boundary data is proportional to $\sin(2\pi x)$. We consider discretizations of size $N = 128, 256, 512$. For a given level of discretization the computational cost of finite difference and wavelet implementations is practically identical. The data for the five-point finite difference method is as follows:

- $\|N256FD - N128FD\| = 5.539$;
- $\|N512FD - N256FD\| = 0.759105$.

The boundary and residual errors are:

- $N = 128$, Boundary error $= 2.491e - 5$, Residual Error $= 7.304e - 5$;

- $N = 256$, Boundary error $= 2.729e - 4$, Residual Error $= 2.921e - 5$;
- $N = 512$, Boundary error $= 3.103e - 12$, Residual Error $= 9.2618e - 12$.

We compare wavelet and finite difference discretizations:

- $\|N128FD - N128D12\| = 2.7576$;
- $\|N256FD - N256D12\| = 0.9232$;
- $\|N512FD - N512D12\| = 0.16639$.

We compare maximum values of the solutions:

- $\|N128FD\| = 3.0885$;
- $\|N256FD\| = 2.8136$;
- $\|N512FD\| = 2.2259$;
- $\|N128D12\| = \|N256D12\| = \|N512D12\| = 2.1212$.

From the above it is obvious that for comparable levels of discretization and computational cost:

- *The wavelet – capacitance matrix method converges spectrally.*
- *The standard finite difference capacitance matrix method converges, at best, marginally.*

We have considered the effect of offsetting the sources from the boundary on the accuracy of the five-point finite difference solution. This produced no measurable effect. That is, the offset and non-offset solutions were practically identical.

Higher order finite difference solutions. We have also considered the effect of using a higher order finite difference approximation on the accuracy of the solution. The five-point approximation of the Laplacian is accurate to order $(\delta x)^2$. We use the nine-point approximation that is accurate to order $(\delta x)^4$.

Without offsetting the results were worse. With offsetting the convergence results improved. That is,

- $\|U128FD - U64FD\| = 3.8190$;
- $\|U256FD - U128FD\| = 0.2273$.

This is a good improvement over the standard five-point finite difference results. However, it is far less accurate than the comparable wavelet results.

We have examined the spectral convergence of a sequence of higher order finite difference approximations for the Helmholtz equation. These are described in Milne [12] for the Laplacian operator. We use offsets of sources that are equal to the supports of the difference operators. These approximations for the Laplacian operator are of order $(\delta x)^k$, $k = 2, 4, 6, 8$, respectively. The approximations are exact for polynomials of degree 3, 5, 7, 9, respectively. In this regard, they correspond to the wavelet–Galerkin approximations for basis $D8$, $D12$, $D16$, $D20$, respectively. We use a discretization of 256 and the notation $N256FDM$ indicates a finite difference solution with discretization 256 and order M. The results are:

- $\|N256FD4 - N256FD2\| = 0.917$;
- $\|N256FD6 - N256FD4\| = 0.0149$;
- $\|N256FD8 - N256FD6\| = 0.00043567$.

The convergence factors are 61.5 and 34.20.

For a comparable degree of approximation, level of discretization, and computational cost, the wavelet–Galerkin solutions have converged faster by several orders of magnitude.

Least-square wavelet methods. We consider solutions with one-half the number of sources in $\hat{\rho}$ and the same boundary discretization and data as shown previously and compare the two solutions. In effect, this procedure transforms the equation for $\hat{\rho}$ from an underdetermined system into an overdetermined system. The minimal norm solution found by singular value decomposition becomes the usual least-square solution.

The notation $N128D12/2$ indicates a solution with a $D12$ basis, a discretization of 128 points on a side, and 64 source points on a side. The results are:

- $\|N128D12 - N128D12/2\| = 6.7e - 6$;
- $\|N128D16 - N128D16/2\| = 6.72e - 8$;
- $\|N128D20 = N128D20/2\| = 2.18e - 8$.

The least-square solutions are, to a tolerance, identical to the full source solutions.

This argues for a certain stability in the algorithm and suggests a new approach to reducing the level of computation while preserving accuracy. We are investigating this further.

Domain shape, boundary data, and rates of convergence. We have examined full source and least-square solutions for the L-shape, T-shape, box, triangle, and wedge. We have considered boundary data of the form $\sin(2\pi x)$ and $\sin(4\pi x)$. Surprisingly, the rates of convergence appear to be independent of domain shape, boundary data, and method (over- or underdetermined systems). The common rates of convergence depend on the scaling function basis and the level of discretization. For a basis DN and discretization δx, the empirical rate of convergence is proportional to $(\delta x)^{N-5}$. We are investigating this further.

4.2. *The Elliptic, or Definite, Case*: $\alpha = 12288$

Figure 14 shows the mesh plots of the solution with $\alpha = 0$ and $\alpha = 1228.8$. Figure 15 shows the mesh plot for $\alpha = 12288$. Since the results are qualitatively similar, we will describe the case $\alpha = 12288$ only. In all cases the boundary data is proportional to $\sin(4\pi x)$.

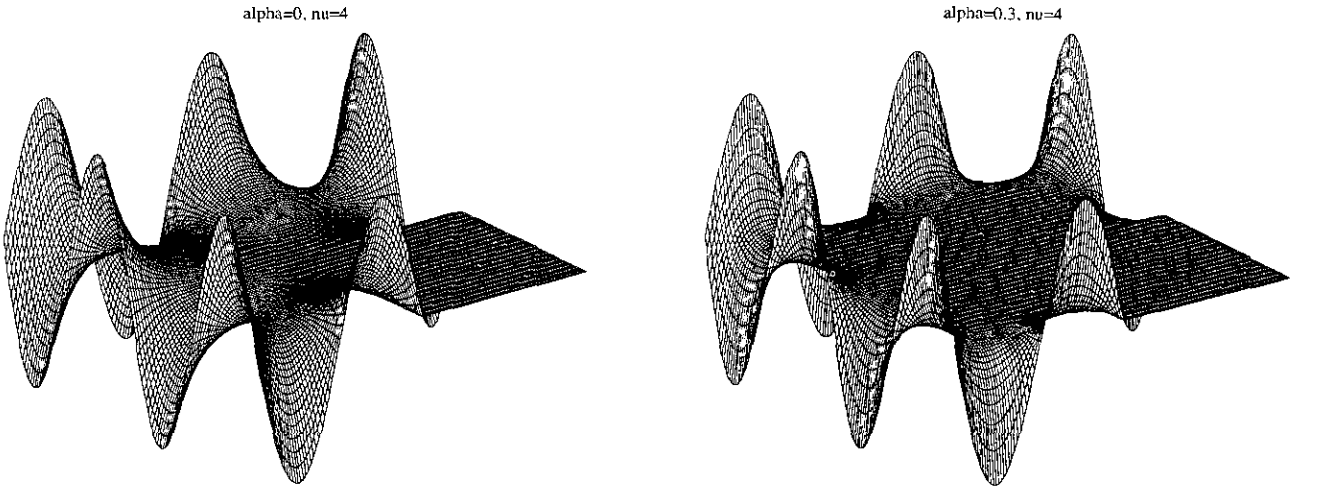

FIG. 14. The mesh plots of the solution with $\alpha = 0$ and $\alpha = 0.3$.

Spectral convergence, $N = 128$. The results are:

- $\|N128D8 - N128D6\| = 0.0281$;
- $\|N128D10 - N128D8\| = 0.008959$;
- $\|N128D12 - N128D10\| = 0.005271$;
- $\|N128D14 - N128D12\| = 0.00103$.

The convergence factors are:

- 3.137;
- 1.6997;
- 5.1175.

Spectral convergence, $N = 256$. The results are:

- $\|N256D16 - N256D12\| = 5.2115e - 5$;
- $\|N256D20 - N256D16\| = 2.8523e - 6$;
- $\|N256D24 - N256D20\| = 4.5015e - 6$.

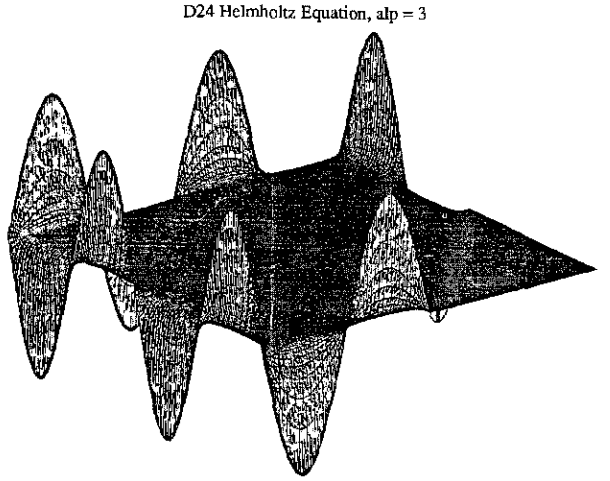

FIG. 15. The mesh plot of the solution with $\alpha = 3$.

For both discretizations the spectral convergence is limited by the elliptic nature of the equation. That is, consistent with the maximum principle of the solution, the magnitude of sources offset sufficiently far from the boundary grow rapidly. Large source values negatively effects the residual and limits the reduction of error possible. This limitation does not appear in the *hyperbolic* problem.

Spectral convergence for the elliptic problem is limited by the maximum principle.

Convergence with discretization. The results are:

- $\|N256D12 - N128D12\| = 0.0073914$;
- $\|N512D12 - N256D12\| = 4.7080e - 5$.

The convergence factor is 156.99.

The convergence with discretization for the elliptic problem is faster than that for the hyperbolic problem.

Some further relevant comparisons are:

- $\|N512D12 - N256D16\| = 5.2044e - 6$;
- $\|N512D12 - N256D20\| = 3.5602e - 6$.

Convergence with finite difference methods. We examine the convergence with discretization of the standard five-point finite difference implementation. The results are:

- $\|U256FD - U128FD\| = 0.008$;
- $\|U512FD - U256FD\| = 0.0021$.

The convergence factor is 3.8095 which is close to the theoretical (optimal) value of 4 with second-order accuracy.

We have also implemented a fourth-order accurate finite difference version of the algorithm. The convergence factor in this case is 1.7. This is less than one half of the second-order value and illustrates the negative effect of boundary residuals on the convergence. In effect, the lower order method will converge faster.

For comparable levels of discretization and computational cost the wavelet–Galerkin implementation converges faster by several orders of magnitude.

Summary. We suggest that our algorithm is an accurate and flexible direct method for solving the Helmholtz equation over all ranges of the parameter and arbitrary non-separable geometries.

5. THE BIHARMONIC HELMHOLTZ EQUATION

We have investigated the numerical solution of the equations describing a thin elastic plate with prescribed loading and nonseparable boundary conditions (geometry). This requires solving the inhomogeneous biharmonic Helmholtz equation

$$(\Delta^2 - k^4)\, U(x, y) = F(x, y)$$

with prescribed displacement and bending moment at the boundary of a nonseparable domain D.

We can solve this equation by a combination of our previous results. That is, we factor the problem as

$$(\Delta + k^2)\, U = V$$
$$(\Delta - k^2)\, V = F$$

with $U = g$ and $V = \Delta U + k^2 U$ on ∂D. We set $F = 0$ and set the bending moment at the boundary equal to zero. Figure 16 shows the solution with $k^2 = 3$, a discretization of $N = 256$ in an L-shape domain.

We find that

$$\|N256D24 - N256D20\| = 8.39343e - 6.$$

6. SYMMETRIES AND THE WAVELET–CAPACITANCE MATRIX

We have also investigated the solutions defined by the eigenstates of the wavelet capacitance matrix. The eigenstates are orthogonal on certain boundaries and induce some remarkable orthogonal fields that are solutions of the harmonic Helmholtz equation. The nature of the resulting collection of solutions is quite interesting and has several applications to the wavelet capacitance matrix method that are currently being investigated.

We consider the Helmholtz operator,

$$H_\alpha = -\Delta + \alpha$$

in a square domain, $\hat{S}$, with Dirichlet boundary conditions. There are common symmetries of operator and domain. These are rotation by 90°, reflection in diagonals, and centerlines. The wavelet–Galerkin discretization finds the capacitance matrix, $\hat{C}$. $\hat{C}$ is real and symmetric with a complete, orthogonal set of n eigenvectors on the discrete boundary, $\hat{B}_n$.

The set of eigenvectors, $\{\hat{V}_j,\ j = 1, ..., n\}$, as boundary data, define solutions $\{\hat{W}_j,\ j = 1, ..., n\}$ of the homogeneous Helmholtz equation in the discrete periodic cell, P. The solutions $\hat{W}$ belong to five mutually orthogonal subspaces defined over the periodic cell. The five subspaces, $\{1, 2, 3, 4, 5\}$, are related to different symmetries of the square. The subspaces are orthogonal over any domain in the periodic cell with the symmetry group of the square, $\hat{S}$.

Figure 17 shows several domains in the periodic cell that have the symmetries of the square. The subspaces are orthogonal over each one and its complement in the periodic cell, P. Therefore, our results apply to many nonseparable domains.

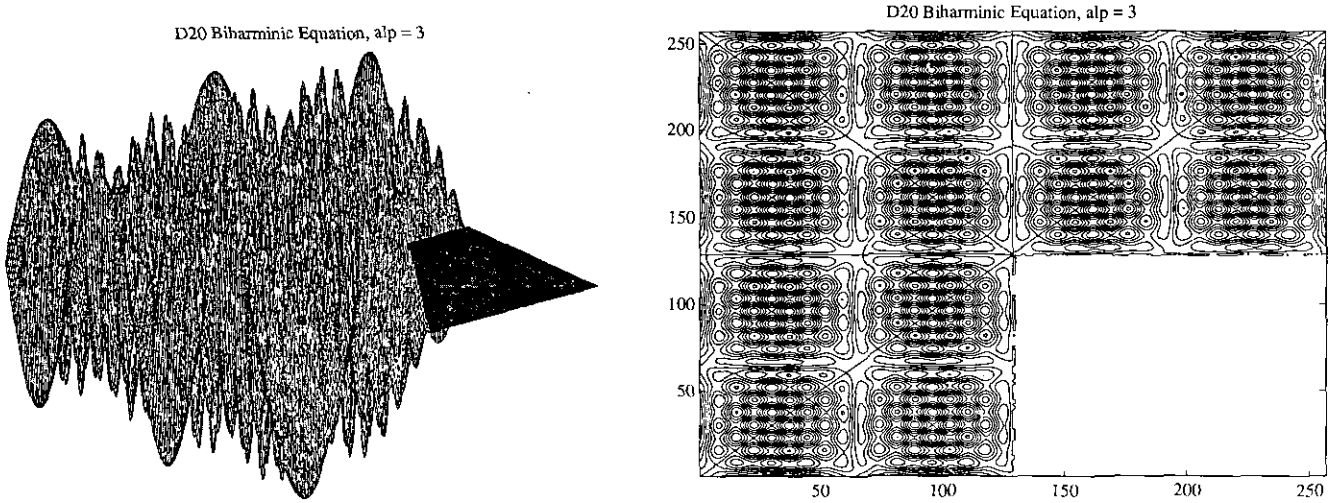

FIG. 16. The contour and mesh plots of the solution to the biharmonic Helmholtz equation in an L-shape domain.

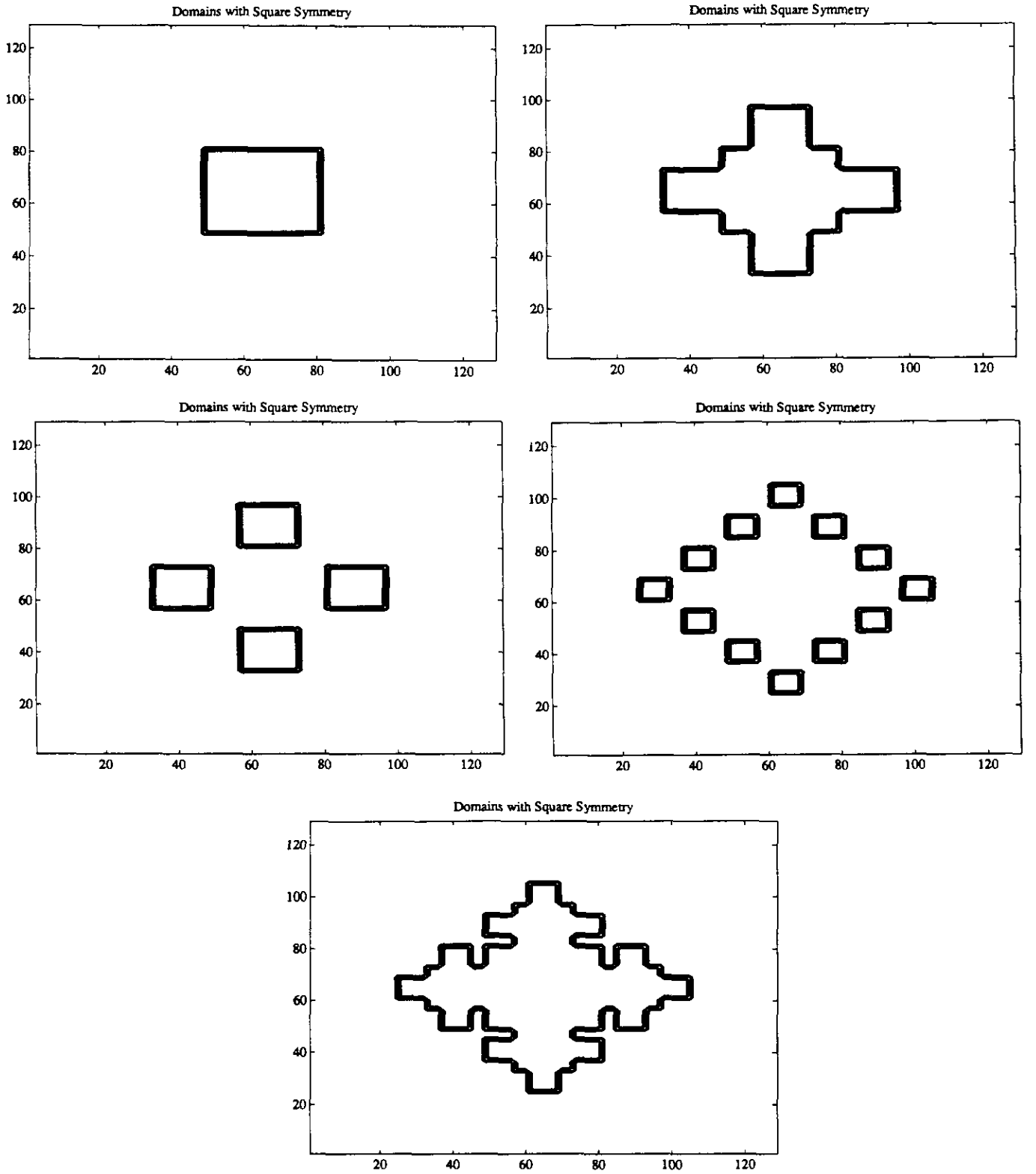

FIG. 17. Several domains in the periodic cell that have the symmetries of the square.

Furthermore, we find that, after discretization:

- The Helmholtz operator, acting on subspaces, preserves orthogonality. That is, $H_\alpha(I) \perp J$, $H_\alpha(I) \perp H_\alpha(J)$ for $I \neq J$.
- The orthogonality structure is independent of the parameter, α. That is, $H_\beta(I_\beta) \perp J_\alpha$, $H_\beta(I_\beta) \perp H_\alpha(J_\alpha)$ for $I \neq J$.
- The discrete orthogonality structures are independent of the scaling function basis used in the wavelet–Galerkin discretization.

Furthermore, the subspaces have an element-wise product structure. The non-orthogonal triple products are:

113	223	333	443
551	552	553	554
124			

The non-orthogonal fourth-order products are

1111	2222	3333	4444	5555
5511	5522	5533	5544	
5512	5513	5514		
5523	5524	5534		
1122	1133	1144	2233	2244
3344	1234			

Non-orthogonal means that the sum over the elements of a field does not vanish. For instance, the product of two fields in subspace 1 belongs to subspace 3, etc. All subspaces are closed under odd-order self-products. Except for space 5, all even-order self-products belong to space 3. The fields in space 3 have non-zero mean. The remaining spaces have zero means. Space 5 contains the fields associated with the double eigenvalues of the capacitance matrix.

The symmetries of the square are directly related to each subspace:

- Fields in space 3 are invariant under rotations of the square, $\hat{S}$, by 90°.
- Fields in space 1 are invariant under rotations of $\hat{S}$ by 180° and reflections in the centerlines.
- Fields in space 2 are invariant under rotations by 90° and reflections in the diagonals and centerlines.
- Fields in space 4 are invariant under rotations by 180° and reflections in the diagonals.
- Fields in space 5, F_5, are transformed into $-F_5$ by rotations of 180°.

Figure 18 shows two fields in subspace 2. The symmetries are clearly visible.

Finally, the size of the (N, N) capacitance matrix, for a uniform discretization of the boundary of the square by N points, occurs in two series, $N = 8k-4$ and $8k$ for $k = 1, 2, \ldots$:

- For $N = 8k-4$, the five spaces $\{1, 2, 3, 4, 5\}$ have $\{k, k-1, k, k-1, 4k-2\}$ elements.
- For $N = 8k$, the five spaces $\{1, 2, 3, 4, 5\}$ have $\{k, k-1, k+1, k, 4k\}$ elements.

Applications. Potential applications of these results include:

- Reduction of capacitance matrix to block diagonal form.
- Systematic and stable offsetting of sources with spectral accuracy (residuals, convergence).
- Definition of high accuracy wavelet element for domain decomposition and the solution of nonlinear systems (Ginzburg–Landau, Euler, Navier–Stokes systems).

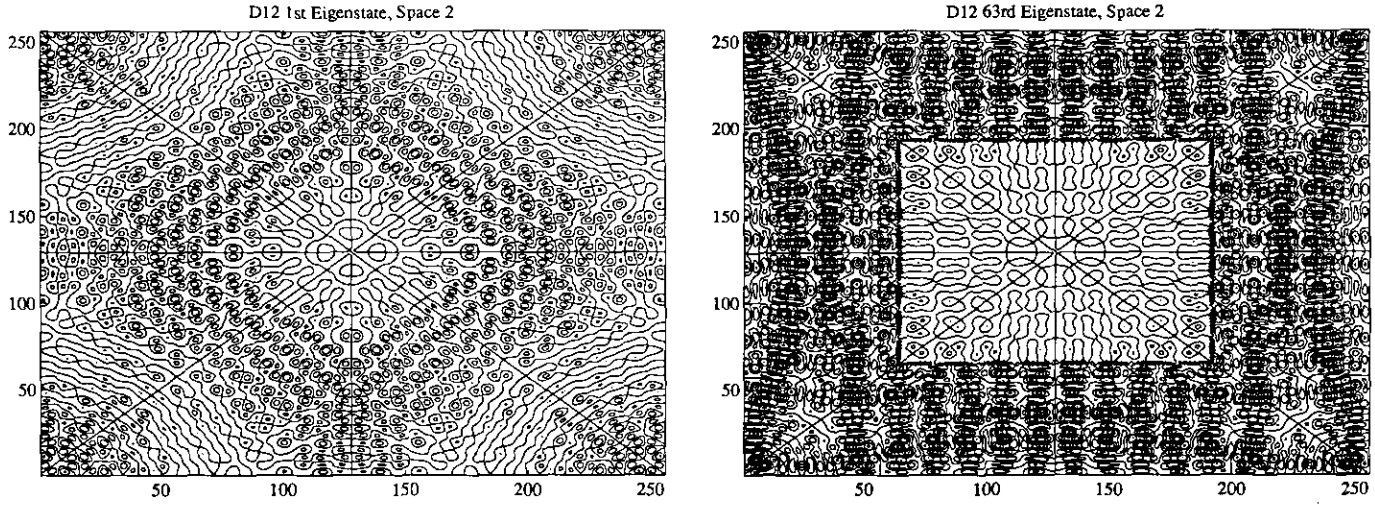

FIG. 18. Two fields in subspace two, associated with eigenstates of the capacitance matrix for the square.

For instance, the nonlinear systems of the nonlinear Schrodinger or Ginzburg–Landau type are generically important in the physics of modulated waves:

$$(-\Delta + v D_t) U + aU + |U|^2 U = 0,$$
$$(-\Delta + v D_t^2) U + aU + |U|^2 U = 0.$$

Substituting $U = \Psi e^{ikt}$, we obtain a nonlinear extension of the Helmholtz equation,

$$(-\Delta + \alpha) \Psi + \Psi^3 = 0.$$

All operations in this equation preserve the subspace (symmetry) structures. We could apply to this system a Galerkin method with fields determined by the capacitance matrix as a basis.

7. SUMMARY

The capacitance matrix method is a fast and the general method for solving boundary value problems in nonseparable domains. It uses fast periodic solvers based on the FFT to drive direct or iterative (conjugate gradient) algorithms. The geometry at the boundary is enforced by potentials with singular support on the boundary. The use of functions with singular support effectively restricts the capacitance matrix method to low order solvers, requiring a high level of discretization to produce accurate results. Due to *boundary residuals*, the introduction of higher order solvers can cause the rate of convergence to become worse. For problems with complicated geometries this fact limits the applicability of the method.

By combining a reformulation of the capacitance matrix method with a wavelet discretization, we have defined a wavelet–capacitance matrix method. This allows the use of higher order approximations with rapid (even spectral) convergence and produces highly accurate solutions for low to moderate levels of discretization. In effect, we have freed the capacitance matrix method of its most serious limitation, while retaining all of the method's advantages.

Our numerical results are for the biharmonic Helmholtz (thin plate) and reduced wave (acoustic) equations in two space dimensions. For low to moderate levels of discretization, accurate solutions were found throughout the parameter range and for several nonseparable domains. Surprisingly, the rate of convergence for our method appears to be independent of the domain shape. Therefore, the results presented here are fairly representative. The method applies equally to equations with three space dimensions and problems with a time dependence. For instance, we have already applied the method to the long time integration of Euler flow, with excellent results.

The symmetries of the operator and domain are preserved by our method. For domains with a high level of symmetry, this allows the accurate numerical resolution of discretely orthogonal spaces that block diagonalize the operator in these domains. These results have interesting applications to domain decomposition, since they allow the definition of highly accurate *wavelet elements* that should be simple to match across element boundaries. The product structure of the orthogonal spaces is useful in the numerical solution of nonlinear systems.

ACKNOWLEDGMENTS

This research was supported in part by the Office of Naval Research under Contract No. N00014-91-C-0086. It was supported in part by the Advanced Research Projects Agency of the Department of Defense and was monitored by the Air Force Office of Scientific Research under Contract No. F49620-89-C-0125.

REFERENCES

1. B. L. Buzbee, F. W. Dorr, J. A. George, and G. H. Golub, *SIAM J. Numer. Anal.* **8**, 722 (1971).
2. B. L. Buzbee and F. W. Dorr, *The Direct Solution of the Biharmonic Equation on Rectangular Regions and the Poisson Equation on Irregular Regions, SIAM J. Numer. Anal.* **11**, 753 (1974).
3. C. Canuto, M. Y. Hussaini, A. Quarteroni, and T. A. Zang, *Spectral Methods in Fluid Dynamics*, Series in Computational Physics (Springer-Verlag, Berlin/Heidelberg, 1988).
4. I. Daubechies, *Commun. Pure Appl. Math.* **41**, 906 (1988).
5. R. Glowinski, "Note on a Multiplier-Fictitious Domain Method for the Numerical Solution of the Dirichlet Problem," Aware Technical Report, 1990 (unpublished).
6. R. Glowinski, W. Lawton, M. Ravachol, and E. Tenenbaum, in *Proceedings, 9th International Conference on Numerical Methods in Applied Sciences and Engineering* (SIAM, Philadelphia, 1990).
7. G. H. Golub and C. F. Van Loan, *Matrix Computations* (The John Hopkins University Press, Baltimore, 1983).
8. R. W. Hockney, *The Potential Calculation and Some Applications, in Methods in Computational Physics* **9**, edited by Alder, Fernbach, and Rotenberg (Academic Press, New York, 1970), p. 248.
9. A. Latto, H. L. Resnikoff, and E. Tenenbaum, Aware Technical Report AD910708, July 1991; in *Proceedings of the French-USA Workshop on Wavelets and Turbulence, Princeton University, June 1991*, edited by Y. Maday (Springer-Verlag, Berlin/New York, 1992).
10. A. Latto and E. Tenenbaum, *Les Ondelettes à Support Compact et la Solution Numérique de l'Equation de Burgers* **311**, 1990, p. 903.
11. E. D. Martin, *Comput. and Fluids* **2**, 79 (1974).
12. W. E. Milne, *Numerical Solution of Differential Equations* (Dover, New York, 1970), p. 130.
13. W. Proskurowski and O. Widlund, *Math. Comput.* **30**, 433 (1976).
14. A. Pares-Sierra and G. Vallis, *J. Comput. Phys.* **82**, 398 (1989).
15. G. Strang, *SIAM Rev.* **31**, 614 (1989).
16. J. Weiss, in *Proceedings, French-USA Workshop on Wavelets and Turbulence, Princeton University, June 1991*, edited by Y. Maday (Springer-Verlag, New York/Berlin, 1992).